Continuous wavelet transform in the analysis of burst synchronization in a coupled laser system

A. Bergner,[1] R. Meucci,[2] K. Al Naimee,[2,3] M. C. Romano,[4] M. Thiel,[4] J. Kurths,[5] and F. T. Arecchi[2,6]

[1]*Center for Dynamics of Complex Systems, University of Potsdam, 14469 Potsdam, Germany*
[2]*CNR-Istituto Nazionale di Ottica Applicata, Largo E. Fermi 6, 50125 Firenze, Italy*
[3]*Department of Physics, University of Baghdad, Baghdad, Iraq*
[4]*College of Physical Sciences, Kings College, University of Aberdeen, Aberdeen AB24 3UE, United Kingdom*
[5]*Potsdam Institute for Climate Impact Research (PIK), 14473 Potsdam, Germany*
[6]*Department of Physics, Università di Firenze, Firenze, Italy*

The transition to synchronization of a pair of coupled chaotic CO_2 lasers is investigated numerically in a model system. This system displays episodes of bursting of different predominant frequencies. Due to the multiple time scales present in this system, we use a complex continuous wavelet transform to perform the synchronization analysis. Thus it enables us to resolve the time of occurrence as well as the frequency of an event in a given time series up to an intrinsic uncertainty. Furthermore, due to the complex nature of that wavelet transform, it yields a direct estimate of the system's phase. We show that, as the coupling strength of the laser system is increased, the mutual coherency increases differently for different frequencies. Additionally we test our method with experimental data.

I. INTRODUCTION

Chaotic synchronization is of fundamental importance in a variety of complex systems [1–3]. Synchronization is often studied in autonomous chaotic systems, that is, systems not subjected to an external driving. In this situation, a coupling between two or more systems (identical or not) can induce changes in some properties of the dynamics of the systems, leading to a common behavior.

Here, we consider the case of synchronization of coupled nonautonomous systems, where chaos is due to an external periodic forcing. In particular, we consider bursting chaotic dynamics originated as a consequence of an interior crisis [4,5]. In contrast to a generic chaotic system, where the attractor is filled almost uniformly in the course of time, in a bursting chaotic dynamics there are rather long time intervals spent around unstable periodic orbits (UPOs) laying inside the basin of attraction of the chaotic attractor before the crisis. The time intervals during which the chaotic orbit is attracted by one of these UPOs lead to bursts of high amplitude, which have the predominant period of the corresponding UPO. Thus, a peculiar feature of a bursting chaotic system is such local structures.

As we couple two such bursting chaotic systems, these local structures can be synchronized. For low values of the coupling strength, they become partially synchronized, and as we increase the coupling strength, they become completely synchronized. In this paper we investigate a model system of two coupled CO_2 lasers, and focus on the role of the different time scales present in the system. For this purpose we utilize a complex continuous wavelet transform to resolve different local structures of this multitime scale system.

The paper is organized as follows. In Sec. II the laser model is presented and the analysis tools are introduced. In Sec. III the results of our analysis are described and in Sec. IV we draw the conclusions.

II. MODEL AND ANALYSIS METHODS

A. Laser model

The model describes a setup of two identical lasers with a common sinusoidal forcing and unidirectional coupling (master-slave coupling). From an experimental point of view such a configuration can be implemented by a single laser whose dynamical regime is controlled via an adequate function generator. Specifically, a master signal is obtained by recording a long time sequence of the laser in a condition where it displays chaotic bursts. In a second stage, the recorded master signal is reproduced by the function generator. The difference signal between the master and the slave laser intensity, amplified by a coupling factor ϵ, is used as an amplitude modulation applied to the sinusoidal driving of the slave laser. This coupling scheme is fairly general allowing coupling between two lasers with nearly identical parameters. The chaotic and synchronization behavior can be reproduced by using the following model of five differential equations for each of the two lasers:

$$\dot{x}_1 = kx_1(x_2 - [1 + \alpha \sin^2(F_x + B)]),$$

$$\dot{x}_2 = -\Gamma_1 x_2 + \gamma x_3 + x_4 + p - 2kx_1 x_2,$$

$$\dot{x}_3 = -\Gamma_1 x_3 + \gamma x_2 + x_5 + p,$$

$$\dot{x}_4 = -\Gamma_2 x_4 + \gamma x_5 + z(x_2 + p),$$

$$\dot{x}_5 = -\Gamma_2 x_5 + \gamma x_4 + z(x_3 + p), \quad (1)$$

where x represents the slave laser and an identical set of equations exists for the master laser y. The coupling and forcing functions are given by
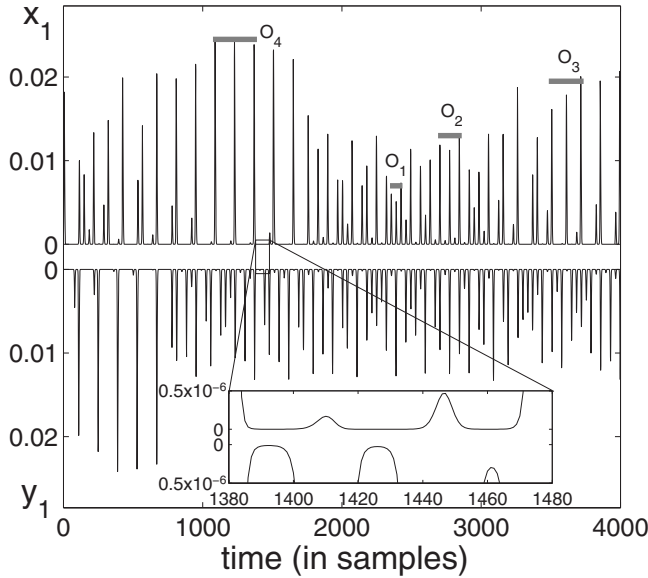
FIG. 1. Time series of the laser intensities x_1 and y_1 from the model system (1) in the uncoupled mode ($\epsilon=0$). The portion of the time series, displayed in the zoomed box, demonstrates that there is a spike on every period of the forcing frequency f. Time durations of local structures are denoted by O_i segments; precisely, O_1, O_2, O_3, and O_4 denote intervals during which the trajectory passes close to an UPO of period 1, 2, 3, 4, respectively. See the text and Fig. 2 for more details.

$$F_x = A\left[1 + \epsilon(y_1 - x_1)\right]\sin(2\pi f t),$$

$$F_y = A\,\sin(2\pi f t). \qquad (2)$$

In the above equations, x_1 represents the laser output intensity, x_2 is the population inversion between the two resonant levels, and x_3, x_4, and x_5 account for molecular exchanges between the two levels, resonant with the radiation field and other rotational levels of the same vibrational band. The parameters of the model are the following: $k=30$ is the unperturbed cavity loss parameter, $\gamma=0.05$ is a coupling constant, $\Gamma_1=10.0643$, and $\Gamma_2=1.0643$ are population relaxation rates, $z=10$ accounts for an effective number of rotational levels, $\alpha=4$ accounts for the efficiency of the electro-optic modulator, $B=0.1794$ is a bias voltage, and $p=0.019\,87$ is the pump rate. The rest of the parameters are related to the external forcing: the frequency $f=1/7$ and the amplitude $A=0.1044$, which are set to a value where the system exhibits chaotic bursting, and ϵ is the master-slave coupling strength. For more details on the model see [6–8].

If the system is uncoupled and autonomous ($A=0$) the subsystems show a fixed point dynamics. When the external forcing is introduced ($A>0$) but without coupling ($\epsilon=0$), the lasers are in a self-sustained regime and show tonic spiking with the frequency f of the periodic forcing (an exemplary time series for each laser is shown in Fig. 1). The spike occurrences of both subsystems are locked perfectly due to their common forcing, however, considering that the initial conditions are different, the spike amplitudes of both systems are uncorrelated. This is the typical behavior of systems which are phase synchronized due to a common driving sig-

nal [2,3]. On a larger time scale, it becomes visible that bursts of higher amplitude—i.e., groups of consecutive spikes with high amplitude—occur repeatedly but irregularly [see time series in Fig. 4(a)]. The creation of these bursts can be explained as follows.

By increasing the amplitude A of the sinusoidal driving, the laser undergoes a sequence of subharmonic bifurcations leading to a small amplitude chaotic attractor. A further increase of A leads to an interior crisis [4,5,9], whereby the chaotic attractor suddenly expands, including phase space regions of other unstable orbits. Shortly after the crisis, an intermittent regime (crisis-induced intermittency) is established where bursts of high amplitude orbits of periods three and four are intercalated with the chaotic attractor before the crisis. The bursting regime investigated here is not a bistable regime. Bistability in this model occurs for lower values of the parameter A (the amplitude of the intrinsic modulation) [10], but we do not consider this regime here.

By introducing the coupling into the system ($\epsilon>0$) we can synchronize both lasers. The synchronization studied here is not the one of the spikes, which are, as already mentioned, locked perfectly, but the synchronization of the bursts, or to be more precise the synchronization of the UPOs of different length. In the numerical system we only observe in-phase synchronization of those orbits, however, in the time series recorded from the experiment we also observe antiphase sychronization during the high amplitude bursts [8].

Due to the strong periodic forcing (2), the rotation times of all orbits are locked to integer factors of the frequency f of the forcing. A spike is created after a full rotation of the trajectory across the attractor. An exhibition of trajectories passing nearby different periodic orbits that exist inside the attractor is presented in Fig. 2. We find segments of orbits, which can have cycling times one to four times the forcing period. Larger spikes (larger values of x_1) are created by orbits with longer periods.

The orbits of different length create the different time scales present in this system, i.e., a multi-time-scale system is generated. A coupling between both laser systems might lead to a synchronization on these different time scales between both systems. With an adjustment of the coupling strength ϵ, the visitings of the UPOs may occur simultaneously in both subsystems, which manifests in a synchronization of the bursts of both lasers. Due to the multiple time scales in this system, which arise from the different UPOs present in the attractor, a continuous wavelet transform represents an appropriate tool for a synchronization analysis.

B. Continuous wavelet transform

The continuous wavelet transform (CWT) has been developed to resolve events localized in time as well as in frequency. It can be interpreted as a constant Q bandpass filter bank ($Q=$ bandwidth/center frequency=const). In mathematical terms the CWT $\mathcal{W}_\psi x$ of a function $x(t)$ is defined as

$$\mathcal{W}_\psi x(\sigma,\tau) := \frac{1}{\sigma}\int_{\mathbb{R}} \psi^*\left(\frac{t-\tau}{\sigma}\right)x(t)dt, \qquad (3)$$

with the mother wavelet $\psi(t)$ translated by τ and dilated by σ. The raised star denotes complex conjugation. The choice
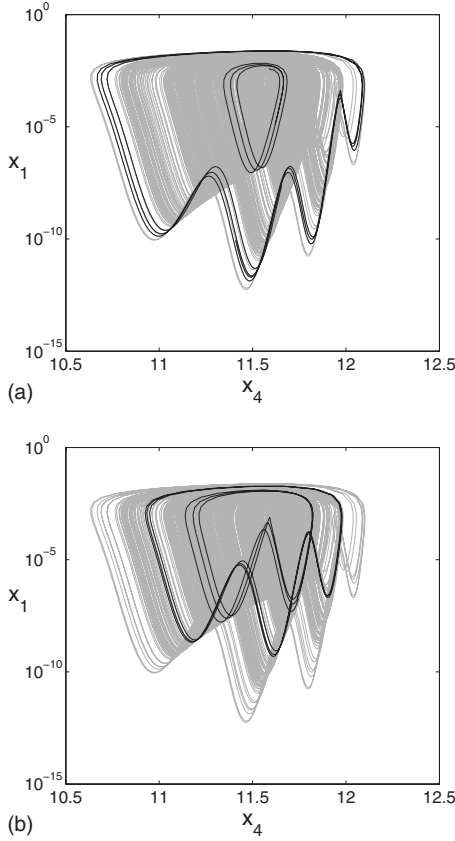
FIG. 2. x_1-x_4 projection of the laser's attractor plotted together with trajectories passing nearby unstable periodic orbits of different length. (a) Orbits of length 1 and 4. (b) Orbits of length 2 and 3.

of the mother wavelet ψ is mainly influencing the time-scale-uncertainty of the resulting wavelet transform. For more background on the CWT see, for example, [11].

The numerical computation of the wavelet transform in this work is performed by using systems of linear difference equations. This approximate method to calculate the CWT has the advantage of a very short computation time, which is also independent of the wavelet's scale. The wavelet used here is given by its z transform

$$\mathcal{Z}\psi = \Psi(z) = H(z)H^*(1/z^*),\qquad(4)$$

with

$$H(z) = \frac{1}{4}\left(\frac{1-p}{z-ip}\right)^3(z^2-1)(z-i),\qquad(5)$$

where $H(z)$ is the system's transfer function and $p \in [0,1]$ is a parameter which allows one to smoothly alter the degree of localization of the wavelet in either time or frequency. However, this method has the drawback that the transformed signal is not completely analytic, and that the wavelet changes its shape slightly under the rescaling process. Nevertheless, if p is choosen high enough ($p > 0.6$), these problems can be neglected. Figure 3 displays the magnitude of the Fourier transform $\Psi(e^{i\omega})$ of this wavelet for $p=0.75$, which is the value that has been used in our analysis. This wavelet can be compared with the Cauchy-Paul-Wavelet. A detailed expla-
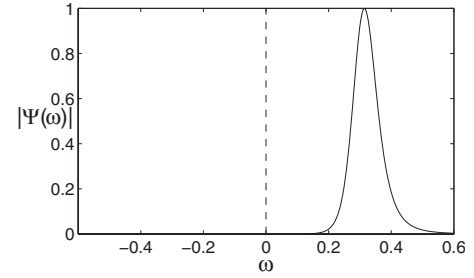

FIG. 3. The magnitude of the Fourier transform $\Psi(\omega)$ of the wavelet (4) for $p=0.75$. Note, that the negative frequencies are basically zero, which gives the wavelet its nice analytic properties.

nation of this wavelet will be given in a forthcoming paper [12].

The complex valued CWT has the advantage over the real valued CWT that it can be immediately split into a phase and an amplitude at each point (σ, τ). Thus the existing methods for detecting phase synchronization can be applied very easily.

C. Measuring synchronization and coherency

Phase synchronization (PS) is characterized by the adaptation of the typical time scales between two systems, while their amplitudes may stay nearly uncorrelated. If one deals with narrow-band oscillatory dynamics, also called phase coherent, simple phase definitions exist, e.g., based on the rotation of the trajectory or based on the Hilbert transform [3,13], that yield good results (see also [14] for a comparison). However, in case of non-phase-coherent dynamics, such as multiple time scales, other approaches are necessary. So far techniques basing on special filters [15], on curvature [16], or on recurrence [17,18] have been proposed. Also in the case of different time scales being present in the system, there is no general method to define the phase of the system. A complex CWT is advantageous for this purpose, because due to its complex nature, it yields a direct estimate of the phase for each time scale of the system. In order to quantify PS, we use two different measures, namely, the mean resultant length (also known as vector strength) and the cross correlation coefficient combined with a complex CWT.

The mean resultant length is defined as follows:

$$r_{xy} := \left|\langle e^{i\Delta\phi_{xy}(t)}\rangle\right| = \left|\frac{1}{T}\sum_{t=1}^{T}e^{i\Delta\phi_{xy}(t)}\right|,\qquad(6)$$

where $\Delta\phi_{xy}(t) := \phi_x(t) - \phi_y(t)$ denotes the phase difference between both systems at time t. We extract the phases $\phi_{x,y}(t)$ directly from the argument of the CWT: $\phi_x(t) = \arg\mathcal{W}_{\psi}x_1(\sigma,t)$, and analogously for y_1. The mean resultant length r_{xy} can assume values from 0 to 1 and quantifies the strength of the mean angle of the circularly distributed values (here the phase differences $\Delta\phi_{xy}$). If $r_{xy}=0$, it indicates that all values of $\Delta\phi_{xy}$ are equally distributed over the interval $[0,2\pi)$, indicating that there is no synchrony between the phases ϕ_x and ϕ_y. The value $r_{xy}=1$ indicates that all phase differences are equal and thus the phase differences are locked perfectly at all times. Since the phases of chaotic

systems usually show a certain amount of phase diffusion, one expects values less than 1, but still considerably larger than 0, if their phases are synchronized. Note that the mean resultant length is similar to the Kuramoto parameter [2,19], but with mean over time instead of being computed over an ensemble of oscillators.

The cross correlation coefficient (CCC) is a linear measure for the similarity between two signals and is given by

$$\rho_{xy} := \frac{\langle xy* \rangle}{\sqrt{\langle |x|^2 \rangle \langle |y|^2 \rangle}}, \qquad (7)$$

where $\langle \; \rangle$ denotes the mean over time and the signals x and y are considered to be mean free. This is the case here, since it is a property of the CWT to remove the mean from signals. In general, ρ_{xy} can be complex valued (in the case of analytic signals) with an arbitrary angle and a modulus between 0 and 1. A modulus of 0 means that there is no linear correlation between the signals, and a value of 1 indicates that the signals are completely linearly correlated, and thus differ only by a factor. The modulus of the complex CCC is also known as coherence.

As Eq. (7) is the normalized scalar product of x and y, thus, the CCC measures the orthogonality between two functions. Since we have that $\langle \sin \omega_1 t, \sin \omega_2 t \rangle = \delta_{\omega_1 \omega_2}$ (where δ_{nm} denotes the Dirac delta) and that PS also implies a coincidence of the frequencies, it is clear that the CCC can be used to detect PS. However, in the case of two real, oscillatory signals the coefficient's modulus fluctuates arbitrarily between 0 and 1 if the phase differences of the two signals are altered. In the extreme case we have $\langle \sin \omega t, \cos \omega t \rangle = 0$, even though intuitively they should be considered to be phase synchronized. In that case one has to calculate the cross correlation function and search the appropriate delay (in the sine-cosine case it is $\pi/2$). This requires much more computations compared to the calculation of the mere CCC, which is the cross correlation function at delay zero.

The complex wavelet used here yields an analytic signal. For analytic signals the phase delay between two signals of equal frequency plays no role, since it can be factored out: $\langle e^{i(\omega t + \phi)}, e^{i\omega t} \rangle = e^{i\phi} \langle e^{i\omega t}, e^{i\omega t} \rangle = e^{i\phi}$. Thus, for analytic signals the CCC is stable under phase shifts and can be used as a measure for PS.

III. RESULTS AND DISCUSSION

Before applying the measures for synchrony and coherency, one needs to consider what the wavelet spectrum reveals and how it can be used together with the above measures to get more insight into the synchronization behavior of the system.

A. Interpretation of the wavelet spectrum

The data has been logarithmized before the computation of the CWT in order to transform the exponentially shaped spikes into a more sinusoidal-like shape (see the time series in Fig. 5 in comparison to the time series in Fig. 1). Thus the resulting wavelet spectrum looks cleaner, since it contains less higher harmonic components. Figure 4 shows an exem-
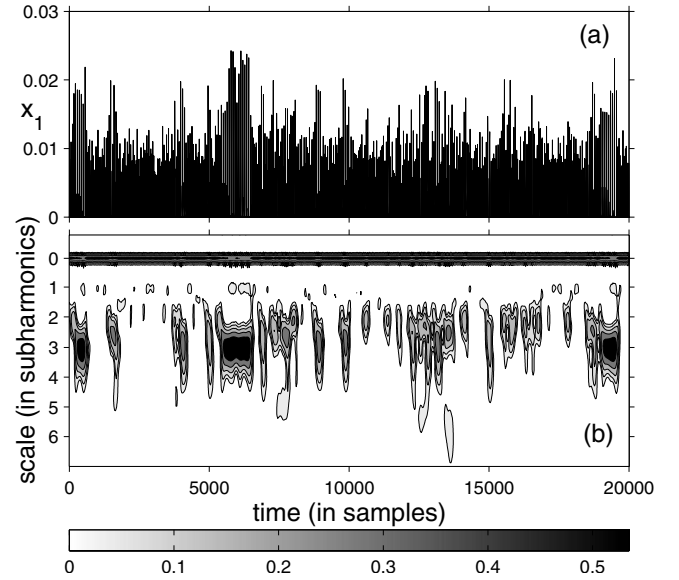

FIG. 4. A time series of the x_1 component of the model system (1) and (2), (a) and the corresponding wavelet power spectrum (b) of the logarithmed data. The spiking frequency f of the laser has been normalized to be scale 0, so that the subharmonics are numbered with 1,2,3,… for the first, second, third, and so on subharmonic, respectively.

plary (original) time series and the corresponding CWT of the logarithmized data.

The continuous horizontal line (normalized to be scale 0) in the CWT of the numerically integrated laser model corresponds to the system's intrinsic spiking frequency f, which is caused by the periodic forcing. On larger scales patches occur at those times where we find bursts in the time series. This can be understood as follows. As we explained in Sec. II, bursts in the time series are created by trajectories passing nearby UPOs with cycling times that are multiples of the forcing's frequency (see again, Fig. 2). Hereby subharmonics of that frequency are created which will become visible as patches at the corresponding scale in the wavelet power spectrum (see Fig. 4, and also Fig. 5, for a magnification of a burst).

Hence, the CWT of the laser model data allows quantifying easily the synchronization between the different time scales and yields a method to indirectly study the synchronization characteristics of the individual periodic orbits.

Figure 6 shows the CWT for a time series recorded from the experiment. The laser intensity signal has been recorded at the onset of the bursting behavior for an amplitude value $A = 0.108$ (such a value is about 3% different from the numerical value). Note that computing the logarithm of the data does not reduce the higher harmonics in the same amount as in the numerical case. The wavelet power spectrum displays higher harmonics of the subharmonics, which appear as patches around scale 0.5.

B. Multiscale synchronization analysis

We combine now the methods of Sec. II to perform a multiscale synchronization analysis. We calculate Eqs. (6)
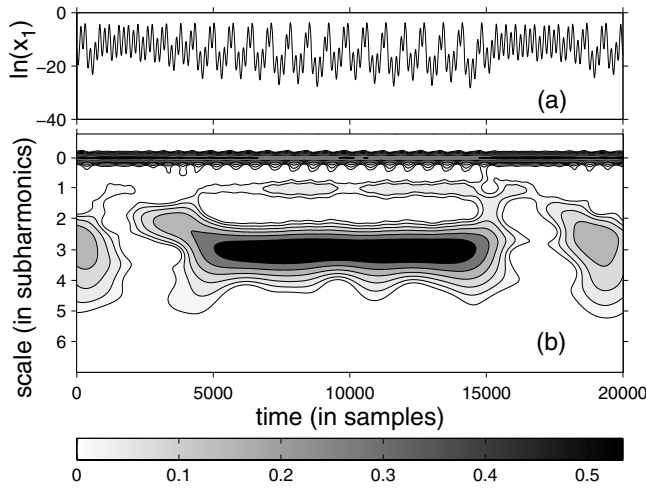
FIG. 5. Magnification of the large burst after sample 5000 in Fig. 4, here with the logarithmed time series in (a). This is a local structure created by the influence of a period four orbit, which becomes visible in the CWT as a third subharmonic.

and (7) for different values of the coupling strength ϵ and for each scale σ of $\mathcal{W}_\psi x_1$ and $\mathcal{W}_\psi y_1$ of the laser intensities from the model system (1) and from experimentally recorded data.

For the model system the measures were calculated for values of ϵ from 0 to 200. The resulting functions $r(\sigma, \epsilon)$ and $|\rho(\sigma, \epsilon)|$ are shown in Fig. 7. Qualitatively, both measures yield similiar results. At $\epsilon \approx 160$, both systems become almost completely synchronized, as it has been already reported in [8]. But here we see in detail that there is almost complete synchronization on all scales.

The result obtained from our analysis is the observation of a diverse transition to synchronization of the coupled model system on its different time scales. In particular, we see an increase of phase coherency among the period three orbits (second subharmonics) between both subsystems for rela-
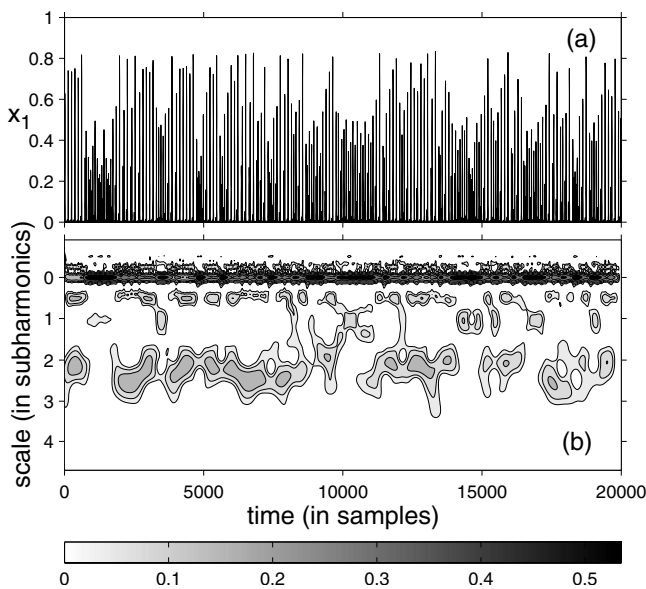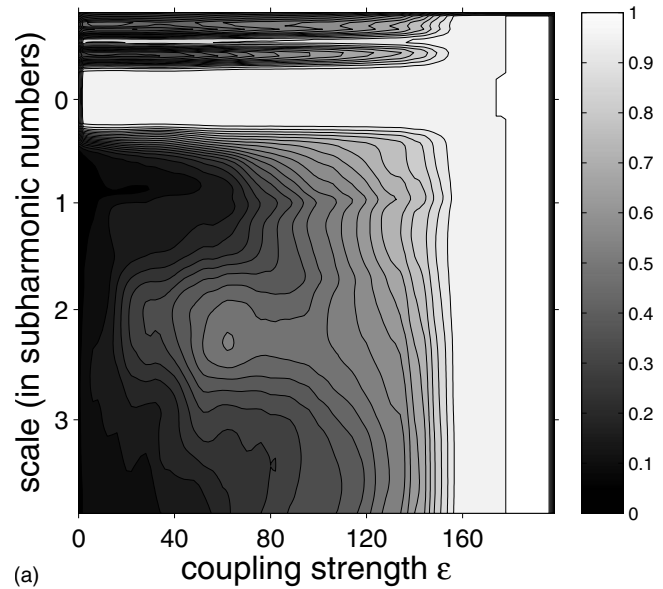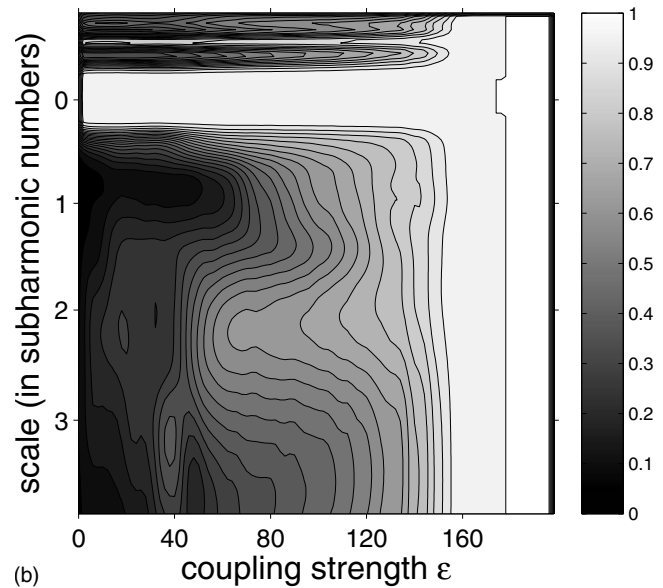

FIG. 6. Same as Fig. 4, but here for experimental data. See the text for more details.

FIG. 7. The results of the multiscale synchronization analysis for the model system (1). Left: the mean resultant length $r(\sigma, \epsilon)$, and right: the modulus $|\rho(\sigma, \epsilon)|$ of the cross correlation coefficient.

tively low values of the coupling strength ϵ, whereas the coherency between the other orbits (period two and four) starts increasing for much higher values of ϵ. This result is obtained with both, the mean resultant length and the correlation coefficient.

Figure 8 shows $r(\epsilon)$ and $|\rho(\epsilon)|$ only for the three subharmonics. Here one can follow the transition to full synchronization for each of those three time scales. Especially for coupling strength bewteen 40 and 80, the difference in the amount of synchrony of the subsystems beween the second and the third subharmonic is rather strong.

In the analysis of experimental data, collected using the master-slave experimental setup described at the beginning of Sec. II, we used three different values of the coupling strength ϵ. Figure 9 shows again both measures of sychronization but here plotted against scale. Both measures reveal
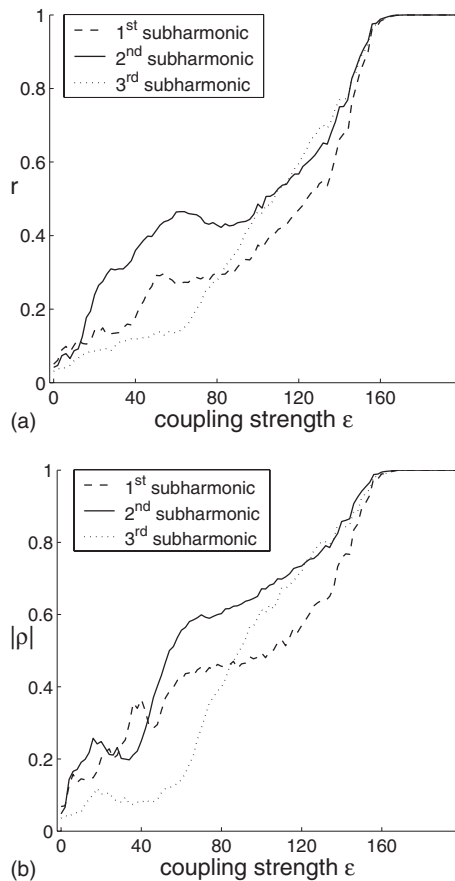
FIG. 8. The measures of synchronization for the model system (1) plotted only for the three subharmonics ($\sigma=1,2,3$). (a) Mean resultant length $r(\epsilon)$ and (b) modulus $|\rho(\epsilon)|$ of the cross correlation coefficient.
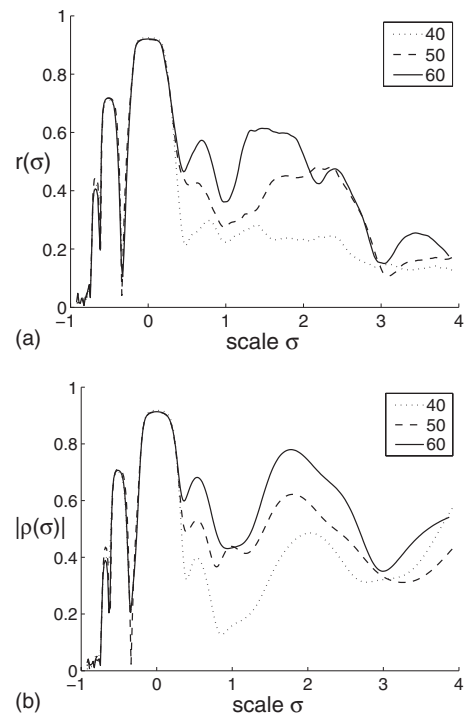

FIG. 9. Results from experimental measurements. (a) The mean resultant length $r(\sigma)$. (b) The modulus $|\rho(\sigma)|$ of the correlation coefficient. The coupling strengths are 40, 50, and 60, respectively.

clearly an increase of synchronization between the second subharmonics of both lasers as the coupling strength is increased. Note that the maxima at $\sigma \approx 0.5$ result from the higher harmonics which have already been discussed in Sec. III A. Further, note that the maxima of the curves are not aligned for the different coupling strengths. This is caused by the fact that we used much less data for the calculation of the presented figures compared to the numerical case. Therefore transients in which the systems are between two orbits and which appear between the subharmonic scales in the CWT have a much larger impact in the statistical analysis. A more detailed discussion of the experiment will be presented elsewhere.

IV. CONCLUSIONS

We have numerically studied the synchronization of bursts in a model system of two externally forced coupled CO_2 lasers with master-slave coupling. The bursts in this system have different predominant frequencies, which arise from unstable periodic orbits of different lengths embedded in the chaotic attractor.

For multi-time-scale systems no standard measures for phase synchronization exist. Therefore we have applied a complex continuous wavelet transform to the data of the lasers' intensities in order to decompose the multiple time scales of that system. We have combined this approach with two measures for phase synchronization, namely, the mean resultant length and the cross correlation coefficient. This procedure enables us to identify details of synchronization of these multi-time-scale systems. In particular, we have found that as we increase the coupling strength, there is an early increase of synchronization between periodic orbits of period three, where the fundamental period is given by the period of the forcing. This insight was not known from previous analysis, carried out with standard methods. This multiple time-scale synchronization analysis has also been tested with experimental data, where we have found qualitatively the same results.

The analysis method presented in this paper can be extended to apply to a general class of multi-time-scale systems, such as neuronal dynamics, where spiking and bursting play a key role in the communication among neurons [20,21].

[1] L. M. Pecora and T. L. Carroll, Phys. Rev. Lett. **64**, 821 (1990).

[2] A. Pikovsky, M. Rosenblum, and J. Kurths, *Synchronization–A Universal Concept in Nonlinear Science* (Cambridge University Press, Cambridge, England, 2001).

[3] S. Boccaletti, J. Kurths, G. Osipov, D. L. Valladares, and C. Zhou, Phys. Rep. **366**, 1 (2002).

[4] C. Grebogi, E. Ott, and J. A. Yorke, Phys. Rev. Lett. **48**, 1507 (1982).

[5] C. Grebogi, E. Ott, and J. A. Yorke, Physica D **7**, 181 (1983).

[6] A. N. Pisarchik, R. Meucci, and F. T. Arecchi, Eur. Phys. J. D **13**, 385 (2001).

[7] R. Meucci, D. Cinotti, E. Allaria, L. Billings, I. Triandaf, D. Morgan, and I. B. Schwartz, Physica D **189**, 70 (2006).

[8] R. Meucci, F. Salvadori, M. V. Ivanchenko, K. A. Naimee, C. Zhou, F. T. Arecchi, S. Boccaletti, and J. Kurths, Phys. Rev. E **74**, 066207 (2006).

[9] C. Grebogi, E. Ott, F. Romeiras, and J. A. Yorke, Phys. Rev. A **36**, 5365 (1987).

[10] R. Meucci, E. Allaria, F. Salvadori, and F. T. Arecchi, Phys. Rev. Lett. **95**, 184101 (2005).

[11] M. Holschneider, *Wavelets: An Analysis Tool* (Oxford University Press, New York, 1995).

[12] A. Bergner and J. Kurths (unpublished).

[13] M. Rosenblum, A. Pikovsky, and J. Kurths, Phys. Rev. Lett. **76**, 1804 (1996).

[14] T. Pereira, M. S. Baptista, and J. Kurths, Phys. Lett. A **362**, 159 (2007).

[15] M. Rosenblum, A. Pikovsky, J. Kurths, G. V. Osipov, I. Z. Kiss, and J. L. Hudson, Phys. Rev. Lett. **89**, 264102 (2002).

[16] G. V. Osipov, B. Hu, C. Zhou, M. V. Ivanchenko, and J. Kurths, Phys. Rev. Lett. **91**, 024101 (2003).

[17] M. C. Romano, M. Thiel, J. Kurths, I. Z. Kiss, and J. L. Hudson, Europhys. Lett. **71**, 466 (2005).

[18] N. Marwan, M. C. Romano, M. Thiel, and J. Kurths, Phys. Rep. **438**, 237 (2007).

[19] Y. Kuramoto, *Chemical Oscillations, Waves, and Turbulence* (Springer-Verlag, Berlin, Heidelberg, 1984).

[20] J. E. Lisman, Trends Neurosci. **20**, 38 (1997).

[21] E. M. Izhikevich, N. S. Desai, E. C. Walcott, and F. C. Hoppensteadt, Trends Neurosci. **26**, 161 (2003).